

# Effects of Magnetic Doping on Weak Antilocalization in Narrow $\text{Bi}_2\text{Se}_3$ Nanoribbons

Judy J. Cha,<sup>†</sup> Martin Claassen,<sup>‡</sup> Desheng Kong,<sup>†</sup> Seung Sae Hong,<sup>‡</sup> Kristie J. Koski,<sup>†</sup> Xiao-Liang Qi,<sup>§,||</sup> and Yi Cui<sup>\*,†,||</sup>

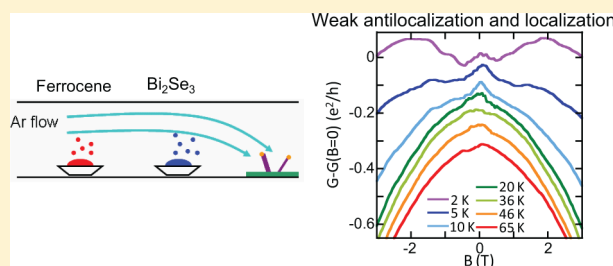
<sup>†</sup>Department of Materials Science and Engineering, <sup>‡</sup>Department of Applied Physics, and <sup>§</sup>Department of Physics, Stanford University, Stanford, California 94305, United States

<sup>||</sup>Stanford Institute for Materials and Energy Sciences, SLAC National Accelerator Laboratory, 2575 Sand Hill Road, Menlo Park, California 94025, United States

## S Supporting Information

**ABSTRACT:** We report low-temperature, magnetotransport measurements of ferrocene-doped  $\text{Bi}_2\text{Se}_3$  nanoribbons grown by vapor–liquid–solid method. The Kondo effect, a saturating resistance upturn at low temperatures, is observed in these ribbons to indicate presence of localized impurity spins. Magnetoconductances of the ferrocene-doped ribbons display both weak localization and weak antilocalization, which is in contrast with those of undoped ribbons that show only weak antilocalization. We show that the observed magnetoconductances are governed by a one-dimensional localization theory that includes spin orbit coupling and magnetic impurity scattering, yielding various scattering and dephasing lengths for  $\text{Bi}_2\text{Se}_3$ . The power law decay of the dephasing length on temperature also reflects one-dimensional localization regime in these narrow  $\text{Bi}_2\text{Se}_3$  nanoribbons. The emergence of weak localization in ferrocene-doped  $\text{Bi}_2\text{Se}_3$  nanoribbons presents ferrocene as an effective magnetic dopant source.

**KEYWORDS:**  $\text{Bi}_2\text{Se}_3$ , topological insulators, magnetic doping, weak antilocalization, nanoribbons



Topological insulators (TIs) possess robust, gapless surface states residing inside a bulk band gap.<sup>1,2</sup> Because of their unique spin-momentum locking property,<sup>3</sup> backscattering of the surface states by nonmagnetic impurities is forbidden by Kramers' theorem.<sup>4</sup> However, the surface states can be gapped by introducing magnetism or superconductivity, in which case new topological phenomena are predicted, such as topological magneto-electric effect,<sup>5,6</sup> quantum anomalous Hall effect,<sup>7</sup> and topological superconductivity with Majorana zero modes.<sup>8</sup> The surface state gap induced by ferromagnetism has already been observed in Fe-doped bulk  $\text{Bi}_2\text{Se}_3$  crystals and Cr-doped  $\text{Bi}_2\text{Se}_3$  thin films via angle-resolved photoemission spectroscopy.<sup>9–11</sup>

A major experimental challenge in realizing the proposed topological phenomena is the existence of residual bulk carriers induced by material imperfections. Transport properties of TI bulk crystals are often dominated by the residual bulk carriers. Therefore TI nanostructures are attractive systems to study the topological surface states due to their large surface-to-volume ratio. Several studies on TI nanostructures include Aharonov-Bohm interference due to the surface conducting electrons,<sup>12,13</sup> consequences of environmental exposure resulting in population of additional electron carriers,<sup>14</sup> and ambipolar field effect via electrostatic gating in thin films and nanoplates,<sup>15–17</sup> all benefited from their nanometer scale. Following this trend, magnetically doped TI nanoribbons can be an ideal platform not only to investigate various theoretical predictions that arise

from breaking the time reversal symmetry, but also to make functional nanodevices that can impact the areas of spintronics.

Previously, Fe-doped  $\text{Bi}_2\text{Se}_3$  nanoribbons were synthesized via vapor–liquid–solid (VLS) growth method using a Fe/Au thin-film catalyst that also served as a dopant source.<sup>18</sup> The Kondo effect was observed in these ribbons due to magnetic impurities. However, the Fe dopant concentration was low, possibly due to the low diffusion constant of Fe, which controls how much Fe can be present in  $\text{Bi}_2\text{Se}_3$  nanoribbons during VLS growth. Ways to increase the dopant concentration were limited because the Fe doping was coupled to the growth substrate temperature. Here, we use ferrocene,  $(\text{Fe}(\text{C}_5\text{H}_5)_2)$ , a metal organic compound with a high vapor pressure, as a dopant source to increase the magnetic dopant concentration in  $\text{Bi}_2\text{Se}_3$  nanoribbons. In this way, the dopant source temperature and the substrate temperature are independently tuned to control the dopant concentration. Magnetotransport measurements of ferrocene-doped, narrow  $\text{Bi}_2\text{Se}_3$  nanoribbons show weak localization (WL) in addition to the usual weak antilocalization (WAL). The measured magnetoconductance is governed by a quasi-one-dimensional (1D) localization

Received: June 6, 2012

Revised: July 18, 2012

theory rather than 2D localization theory, consistent with the narrow width of the ribbon. In some ribbons, negative magnetoresistance extends to high magnetic fields, suggesting additional transport regimes not captured by the 1D localization theory.

$\text{Bi}_2\text{Se}_3$  nanoribbons were grown on Si substrates via the VLS mechanism using  $\text{Bi}_2\text{Se}_3$  powder as source and a 10 nm Au film as metal catalyst in a horizontal tube furnace.<sup>19</sup> Ferrocene powder was loaded in the upstream region of the quartz tube, 7–8 in. away from the center. The optimal growth conditions were  $\text{Bi}_2\text{Se}_3$  source temperatures between 530 and 560 °C, ferrocene temperatures between 50–130 °C, and substrate temperatures of 350–450 °C under a constant flow of high purity Ar gas at 130 standard cubic centimeters per minute at 3.6 Torr for 2–3 h (Figure 1a, schematic of the growth setup).

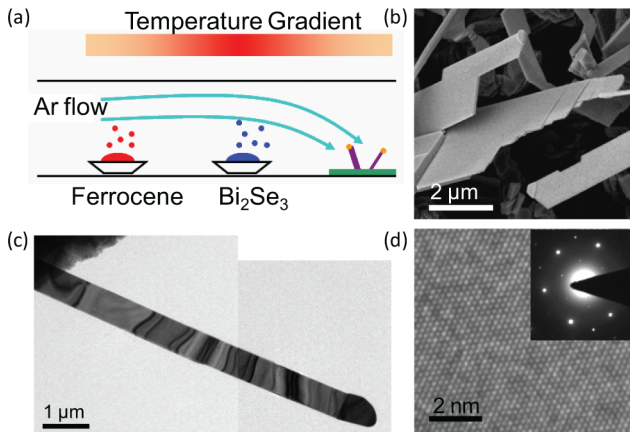


**Figure 1.** Synthesis of ferrocene-doped  $\text{Bi}_2\text{Se}_3$  nanoribbons. (a) Schematic of the growth setup where the ferrocene and  $\text{Bi}_2\text{Se}_3$  powders are used as the dopant and source materials in a horizontal tube furnace. (b) Scanning electron micrograph of the ribbons grown at 560 °C  $\text{Bi}_2\text{Se}_3$  source temperature and 50 °C ferrocene dopant temperature. (c) TEM image of a ferrocene-doped ribbon. (d) High-resolution TEM image and selected area diffraction pattern (inset) of the ribbon shown in (c).

The morphology and the crystal structure of the ribbons are identical to  $\text{Bi}_2\text{Se}_3$  nanoribbons (Figure 1b–d),<sup>19</sup> and ribbon surfaces are smooth with no byproduct like Fe particles (Figure 1c). High-resolution transmission electron microscope (TEM) images show lattice fringes matching those of  $\text{Bi}_2\text{Se}_3$  without any obvious small Fe clusters embedded inside (Figure 1d). X-ray diffraction data from a growth substrate matches the crystal structure of  $\text{Bi}_2\text{Se}_3$ . Energy dispersive X-ray spectroscopy in TEM showed a small Fe peak from these ribbons (Supporting Information Figure S1), however accurate dopant concentrations could not be obtained due to often present Fe background signals, coming from the microscope.

Magnetic dopants in these  $\text{Bi}_2\text{Se}_3$  nanoribbons were confirmed by the emerging Kondo effect, a universal signature of magnetic interactions among electrons in conductors.<sup>20</sup> Temperature-dependent, 4-point resistance down to 2 K was measured from four devices, one undoped and three ferrocene-doped  $\text{Bi}_2\text{Se}_3$  nanoribbons for comparison, using a Physical Property Measurement System (Quantum Design) and an Oxford  $^4\text{He}$  cryostat. The devices were fabricated using standard e-beam lithography, followed by thermal evaporation of Cr/Au contacts. The undoped  $\text{Bi}_2\text{Se}_3$  ribbon (device S1, Figure 2a) shows a typical temperature response of a metal,

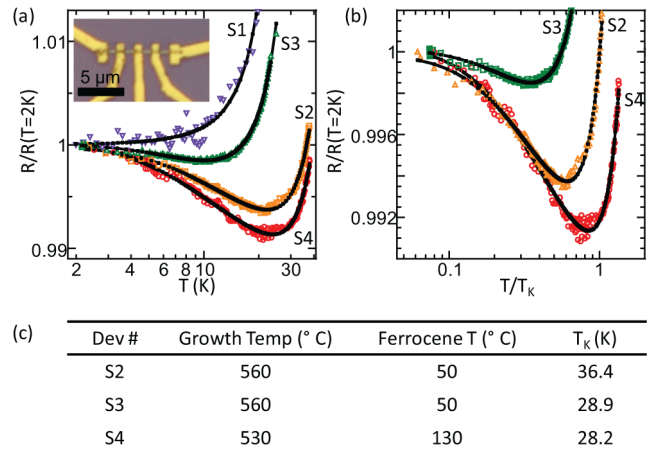


**Figure 2.** (a) Longitudinal resistances of undoped (S1) and ferrocene-doped (S2–S4)  $\text{Bi}_2\text{Se}_3$  nanoribbons as a function of temperature down to 2 K. The inset shows an optical image of device S2. Solid curves are fits using eq 1. (b) Resistances of device S2–S4 normalized to  $R$  at 2 K, plotted against  $T/T_K$ . (c) Growth conditions for device S2–S4 and the Kondo temperature,  $T_K$ , obtained from the fit in eq 1.

whereas ferrocene-doped ribbons (devices S2–S4, Figure 2a) exhibit a saturating resistance upturn at low temperature, a characteristic feature of the Kondo effect arising from magnetic impurities. Saturating resistance upturn may also be observed in samples free of magnetic dopants, for example in  $\text{Bi}_2\text{Te}_3$  nanoribbons and  $\text{Bi}_2\text{Se}_3$  bulk crystals,<sup>13,21</sup> when the Fermi level is close to the conduction band bottom. In our case, however, magnetoconductance measurements also support presence of magnetic impurities. Thus, we describe the temperature-dependent resistance using a simplified Kondo model

$$R(T) = R_0 + qT^2 + pT^5 + R_K \left( \frac{T}{T_K} \right) \quad (1)$$

where  $R_0$  is the residual resistance due to disorder,  $T^2$  and  $T^5$  terms represent electron–electron and electron–phonon interactions respectively, and  $R_K(T/T_K)$  captures the Kondo effect with Kondo temperature,  $T_K$ . To fit the data, we used an empirical form,  $R_K(T/T_K) = R_K(T=0) [T_K'^2 / (T^2 + T_K'^2)]^s$  where  $T_K' = T_K / (2^{1/s} - 1)^{1/2}$  with  $s$  fixed at 0.225.<sup>22,23</sup> Fitting the resistances of device S2–S4 with eq 1 yielded  $T_K$ 's ranging between 28 and 36 K (Figure 2c, Supporting Information, Table S1). In the Kondo regime, the resistance is a universal function of  $T/T_K$ . The normalized resistances of device S2 and S4 overlap nicely below  $T/T_K < \sim 0.6$  when plotted against  $T/T_K$ , but device S3 does not (Figure 2b), suggesting additional magnetic interactions for device S3.

To examine how the magnetic impurities may affect the TI surface states, we first discuss magnetotransport of undoped  $\text{Bi}_2\text{Se}_3$  nanoribbons. We measured conductance of device S1 in magnetic fields up to 8 T at several angles between the direction of the magnetic field and the basal plane of the ribbon (schematic in Figure 3a inset). For all angles, a pronounced peak is observed in conductance at small fields (Figure 3a, full traces in Supporting Information, Figure S2). This is WAL, a positive quantum correction to the classical magnetoconductivity, and is expected in TIs due to the helical surface states.<sup>24,25</sup> Presence of a shallow, broad peak at 90° (parallel magnetic field) suggests that in addition to the surface states the bulk spin orbit coupling (SOC) also contributes to WAL

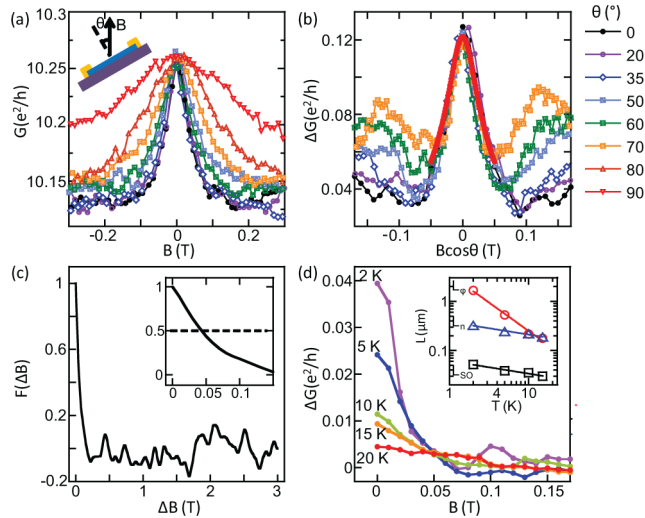


**Figure 3.** (a) Magnetoconductances of device S1 at multiple angles between the magnetic field and the basal plane of Bi<sub>2</sub>Se<sub>3</sub>. The geometry is shown in the inset. (b) After subtracting the parabolic background and 90° conductance trace, the conductance changes are plotted against  $B \cos \theta$ . The red curve is a fit to the 0° conductance change using eq 2, yielding  $L_n = 246.9$  nm,  $L_\phi = 395.6$  nm, and  $L_{SO} = 39.7$  nm. (c) Autocorrelation of the 0° conductance after subtracting the parabolic background. Inset is a zoom-in near zero  $\Delta B$ .  $B_c = 0.043$ , yielding  $L_\phi = 302.3$  nm. (d) Magnetoconductances of another undoped Bi<sub>2</sub>Se<sub>3</sub> nanoribbon device at temperatures ranging between 2 and 20 K. The inset shows  $L_n$  (triangles),  $L_\phi$  (circles), and  $L_{SO}$  (squares) as a function of temperature in log–log scale. The lines are power law fits, yielding  $L_n \sim T^{-0.26}$ ,  $L_\phi \sim T^{-1.15}$ , and  $L_{SO} \sim T^{-0.26}$ .

but with much weaker strength. Assuming isotropic bulk contribution, the 90° conductance and parabolic conductance background were subtracted from the rest of conductance traces, which were then plotted against  $B \cos \theta$  (Figure 3b). All traces overlay to a single curve at small fields, indicating the surface origin of the magnetoconductance. Similar angle-dependent studies were carried out in Bi<sub>2</sub>Te<sub>3</sub> thin films and Bi<sub>2</sub>(Se<sub>x</sub>Te<sub>1-x</sub>)<sub>3</sub> nanostructures.<sup>26,27</sup>

We use a quasi-1D localization theory to fit the observed WAL in device S1, instead of the 2D localization theory described by the Hikami–Larkin–Nagaoka equation,<sup>24</sup> because the width of the ribbon ( $W = 139$  nm) is smaller than the typical dephasing length,  $L_\phi \sim 300$  nm, for Bi<sub>2</sub>Se<sub>3</sub>.<sup>28–30</sup> We checked that the 2D localization theory did not apply in this case because fitting the data with the 2D theory yielded  $\alpha$  of  $-8.6$ , an unphysical value compared to the reported range of  $-0.4$  and  $-1.1$  for Bi<sub>2</sub>Se<sub>3</sub> and Bi<sub>2</sub>Te<sub>3</sub> (detailed analysis in Supporting Information).<sup>28–30</sup> A 1D localization theory that considers electron–electron interactions in the presence of magnetic fields has been developed previously.<sup>31,32</sup> Here, to describe magnetically doped, narrow Bi<sub>2</sub>Se<sub>3</sub> nanoribbons, we derive a full description of the localization in 1D, including scatterings from SOC (decay time,  $\tau_{SO}$ ) and magnetic impurities (decay time,  $\tau_m$ , assuming frozen impurity spins on the time scale of a scattering process)

$$\Delta\sigma_1 = \frac{\sqrt{2} e^2 L_n}{\pi \hbar L} \left[ \frac{3}{2} \frac{\text{Ai}\left(\frac{2L_n^2}{L_1^2}\right)}{\text{Ai}'\left(\frac{2L_n^2}{L_1^2}\right)} - \frac{1}{2} \frac{\text{Ai}\left(\frac{2L_n^2}{L_2^2}\right)}{\text{Ai}'\left(\frac{2L_n^2}{L_2^2}\right)} \right] \quad (2)$$

where  $\Delta\sigma_1$  is the conductance quantum correction in 1D,  $L$  and  $L_n$  are the ribbon length and the Nyquist length, respectively, Ai represents the Airy function,  $L_1 = (4/(3D\tau_{SO}) + 1/(D\tau_\phi) + 2/(3D\tau_m))^{-1/2}$ , and  $L_2 = (1/(D\tau_\phi) + 2/(D\tau_m))^{-1/2}$ .  $D$  denotes the diffusion constant and the dephasing decay time,  $\tau_\phi$ , depends on the magnetic field,  $1/\tau_\phi = 1/(\tau_\phi(B=0)) + 1/\tau_H$  where  $\tau_H = (12L_H^4)/DW^2$  and  $L_H = (\hbar/2eB)^{1/2}$ . For undoped Bi<sub>2</sub>Se<sub>3</sub> nanoribbons,  $L_m$  is infinite since it is inversely proportional to the magnetic impurity concentration, and for simplicity we assume that  $\tau_{SO} \ll \tau_\phi$ <sup>29</sup> so that  $L_1 = (4/(3D\tau_{SO}))^{-1/2}$  and  $L_2 = (1/(D\tau_\phi))^{-1/2}$ . The red curve in Figure 3b is the fit to 0° conductance correction using eq 2, yielding  $L_n = 246.9$  nm,  $L_\phi = 395.6$  nm, and  $L_{SO} = 39.7$  nm (note  $L_x = (D\tau_x)^{1/2}$ ). Fitting eq 2 to remaining conductance traces also yielded similar values for  $L_n$ ,  $L_\phi$ , and  $L_{SO}$  (Supporting Information, Table S2). For example, the fit to 20° conductance correction gave  $L_n = 286.0$  nm,  $L_\phi = 400.7$  nm, and  $L_{SO} = 46.0$  nm. We note that  $L_{SO} \ll L_\phi$ , which is in agreement with our assumption that  $\tau_{SO} \ll \tau_\phi$ . As a check,  $L_\phi$  was obtained alternatively from the universal conductance fluctuations.<sup>33</sup> Figure 3c shows the autocorrelation function of the 0° conductance after the parabolic background subtraction,  $F(\Delta B) = \langle \Delta G(B)\Delta G(B + \Delta B) \rangle$ . At  $\Delta B = \Delta B_c$ ,  $F(\Delta B_c) = F(0)/2$  where  $B_c = 0.95(\hbar/e)(1/L_\phi^2)$ .<sup>33,34</sup> We obtain  $B_c = 0.043$ , corresponding to  $L_\phi = 302.3$  nm. Repeating the analysis on all conductance traces gave the average  $L_\phi$  of  $314 \pm 14$  nm, comparable to the  $L_\phi$  obtained using the 1D localization theory. Values of  $L_\phi$  and  $L_{SO}$  presented here are in agreement with other reported values of  $L_\phi$  and  $L_{SO}$  of Bi and Bi<sub>2</sub>Se<sub>3</sub> thin films.<sup>29,30,33</sup>

Another narrow, undoped Bi<sub>2</sub>Se<sub>3</sub> nanoribbon device was measured at temperatures ranging from 2 to 20 K to confirm that the observed WAL is confined in 1D.  $L_n$  should decay as  $T^{-1/3}$  in 1D and  $T^{-1/2}$  in 2D.<sup>31,35</sup> Parabolic-background subtracted, symmetrized magnetoconductances were fitted to eq 2 to obtain  $L_n$ ,  $L_\phi$  and  $L_{SO}$  (Figure 3d, fit not shown.). All scattering lengths decrease at higher temperatures due to the increased thermal scattering and  $L_n$  decays as  $\sim T^{-0.26}$  (Figure 3d inset), closer to that of the 1D localization theory than 2D. Thus, for ribbons whose width is narrower than  $L_\phi$ , eq 2 describes WAL well.  $L_\phi$  is proportional to  $\sim T^{-1.15}$  and decreases much faster than  $L_n$  and  $L_{SO}$  at higher temperatures. We note that  $L_\phi \sim T^{-1}$  indicates electron–electron collisions with large energy transfers.<sup>35</sup>

We now turn our attention to magnetotransport of the ferrocene-doped Bi<sub>2</sub>Se<sub>3</sub> nanoribbons. In particular, we focus on how WAL is affected by the magnetic impurities. Magnetoconductances of device S2 and S3 were measured at temperatures ranging between 2 and 65 K (Figure 4a,b). Instead of a single peak representative of WAL, more complicated traces were observed. We first analyze device S2 (Figure 4a). The magnetoconductance of device S2 at 2 and 5 K appears to be a combination of WL and WAL, an effect expected in TIs if magnetic impurities open a band gap in the surface state.<sup>36</sup> Alternatively, magnetic impurities can effectively cancel out the bulk SOC, inducing the observed mixture of WL and WAL. Much more rigorous transport studies are necessary to decipher a band gap opening due to magnetic impurities, which is beyond the scope of this work. After subtracting the classical magnetoconductance background, the 2 K conductance trace was fitted with eq 2 to obtain  $L_m$ . To reduce a number of free parameters,  $L_\phi$  was fixed at 400 nm, based on the WAL analysis of the undoped Bi<sub>2</sub>Se<sub>3</sub> nanoribbons, while  $L_n$ ,  $L_{SO}$ , and  $L_m$  were free to change. Fitting was not so robust as eq

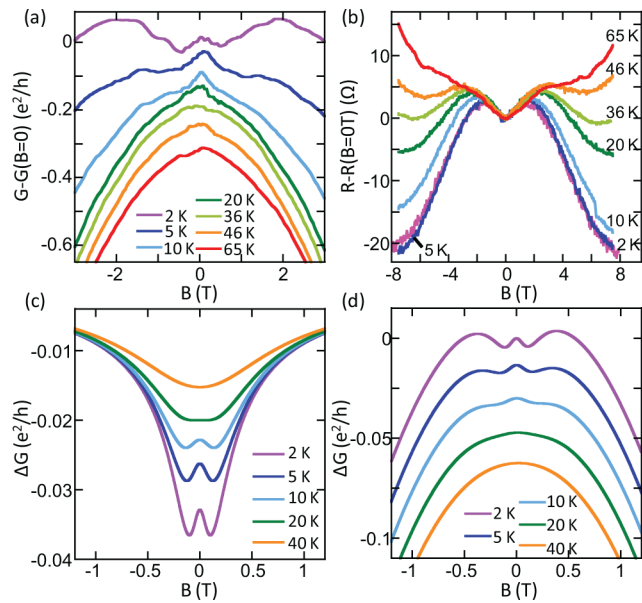


**Figure 4.** (a) Magnetococonductances of device S2 and (b) magnetoresistances of device S3 at temperatures ranging from 2 and 65 K. Traces in (a) are displayed with offsets for visual clarity. (c) Calculated magnetococonductance corrections at different temperatures, using eq 2 with the following parameters:  $L_n = 30$  nm,  $L_{SO} = 40$  nm,  $L_m = 400$  nm, and  $L_\phi = 400$  nm at 2 K.  $L_n$  and  $L_{SO}$  decrease as  $T^{-0.26}$  while  $L_\phi$  as  $T^{-1.15}$ . (d) Calculated magnetococonductances with parabolic background at different temperatures. Parameters are the same as those in (c). Traces are displayed with offsets for visual clarity.

2 consists of two rapidly changing terms with opposite signs and three free parameters (Supporting Information, Figures S3 and S4). Nonetheless, it is clear that magnetic impurities induce coexistence of WL and WAL, and that eq 2 correctly captures the physics. The closest fit yields  $L_n = 30$  nm,  $L_{SO} = 24$  nm, and  $L_m = 430$  nm. We note that changes in  $L_\phi$  alone, in particular possible reduction in  $L_\phi$  due to increased disorder by the dopants, cannot induce coexistence of WL and WAL, as observed in various transport studies that show only WAL in topological insulators that are doped with nonmagnetic impurities (Supporting Information, Figure S5).<sup>26,27,37</sup> At higher temperatures (10 and 20 K), WL appears to diminish while WAL persists. At temperatures  $>20$  K, the quantum corrections to the magnetoconductance are lost due to increased thermal scattering, and only the classical parabolic magnetoconductance is observed.

The balance between WL and WAL as a function of temperature in the presence of magnetic impurities was reproduced using eq 2. For illustration, we set  $L_n = 30$  nm,  $L_{SO} = 40$  nm,  $L_m = 400$  nm, and  $L_\phi = 400$  nm at 2 K, and let  $L_n$ ,  $L_{SO}$ , and  $L_\phi$  decay as  $T^{-0.26}$ ,  $T^{-0.26}$ , and  $T^{-1.15}$ , respectively as obtained from the temperature-dependent WAL study (Figure 3d). The quantum correction to conductance,  $\Delta G$ , is negative due to  $L_m$  and its shape indicates competition between WL and WAL (Figure 4c). Adding the quantum correction to classical parabolic background, taken from the 65 K conductance trace, gives calculated conductance traces (Figure 4d), whose overall shape resembles acquired data shown in Figure 4a. We note that a suppression of WAL and a cross over from WAL to WL have been observed in Fe-decorated  $\text{Bi}_2\text{Te}_3$  thin films<sup>26</sup> and Cr-doped  $\text{Bi}_2\text{Se}_3$  thin films,<sup>11</sup> where the 2D localization theory by the Hikami–Larkin–Nagaoka equation<sup>24</sup> was used to describe

the behavior. Another device that shows the mixed WL and WAL is presented in Supporting Information, Figure S6.

In contrast to the mixed WL and WAL effects seen in device S2, negative magnetoresistance ( $\sim 2\%$  change) extending to high magnetic fields ( $\sim 8$  T) is observed in device S3 (Figure 4b). Consistently, the temperature-dependent resistance curve of device S3 did not fall on the universal Kondo curve (Figure 2b), indicating additional transport process from magnetic impurities beside localization effects. The exact mechanism for this behavior is unclear, but the different transport between device S2 and S3 suggests a range of magnetic dopant levels in  $\text{Bi}_2\text{Se}_3$  nanoribbons even under the same growth conditions. At higher temperatures, thermal fluctuations dominate, thus the negative resistance starts to decrease.

In conclusion,  $\text{Bi}_2\text{Se}_3$  nanoribbons were magnetically doped using the metal organic compound ferrocene. The presence of magnetic impurities in ferrocene-doped  $\text{Bi}_2\text{Se}_3$  nanoribbons was confirmed by the emerging Kondo effect with the Kondo temperature ranging between 28 and 36 K. Additionally, a mixture of WL and WAL was observed. The 1D localization theory describes the observed magnetotransport well and yielded various scattering lengths such as  $L_\phi$ ,  $L_{SO}$ , and  $L_m$  for  $\text{Bi}_2\text{Se}_3$ . In some ribbons, negative magnetoresistance was observed in high magnetic fields, perhaps suggesting different magnetic impurity levels. Unfortunately, no other magnetic orderings were observed in these systems. In thin film studies, Cr-doped  $(\text{Bi,Sb})_2\text{Te}_3$  thin films show anomalous Hall effect while Cr-doped  $\text{Bi}_2\text{Se}_3$  thin films do not, although the magnetic dopant concentrations and bulk electron densities of the two systems are comparable.<sup>11,38</sup> Therefore, particular material properties may play an important role in realizing magnetic ordering of impurities in topological insulators.

## ■ ASSOCIATED CONTENT

### 📄 Supporting Information

Energy dispersive X-ray spectrum of a ferrocene-doped  $\text{Bi}_2\text{Se}_3$  nanoribbon, Kondo analysis, angle-dependent magnetoresistance up to 8 T of an undoped  $\text{Bi}_2\text{Se}_3$  nanoribbon, temperature-dependent weak antilocalization of an undoped  $\text{Bi}_2\text{Se}_3$  nanoribbon, balance between weak localization and antilocalization in ferrocene-doped  $\text{Bi}_2\text{Se}_3$  nanoribbons, weak antilocalization in Pb- and Sn-doped  $\text{Bi}_2\text{Se}_3$  nanoribbons, and transport of additional ferrocene-doped  $\text{Bi}_2\text{Se}_3$  nanoribbons. This material is available free of charge via the Internet at <http://pubs.acs.org>.

## ■ AUTHOR INFORMATION

### Corresponding Author

\*E-mail: yicui@stanford.edu.

### Notes

The authors declare no competing financial interest.

## ■ ACKNOWLEDGMENTS

The authors thank C. D. Wessells for X-ray diffraction measurements on ferrocene-doped  $\text{Bi}_2\text{Se}_3$  nanoribbons and K. Lai for helpful discussions. This work was supported by the Keck Foundation and a DARPA MESO project (no. N66001-11-1-4105). The manuscript was written through contributions of all authors. All authors have given approval to the final version of the manuscript.

## REFERENCES

- (1) Hasan, M. Z.; Kane, C. L. *Rev. Mod. Phys.* **2010**, *82*, 3045–3067.
- (2) Qi, X.-L.; Zhang, S.-C. *Rev. Mod. Phys.* **2011**, *83*, 1057–1110.
- (3) Raghu, S.; Chung, S. B.; Qi, X.-L.; Zhang, S.-C. *Phys. Rev. Lett.* **2010**, *104*, 116401.
- (4) Kane, C. L.; Mele, E. J. *Phys. Rev. Lett.* **2005**, *95*, 146802.
- (5) Qi, X.-L.; Hughes, T. L.; Zhang, S.-C. *Phys. Rev. B* **2008**, *78*, 195424.
- (6) Qi, X.-L.; Li, R.; Zang, J.; Zhang, S.-C. *Science* **2009**, *323*, 1184–1187.
- (7) Yu, R.; Zhang, W.; Zhang, H.-J.; Zhang, S.-C.; Dai, X.; Fang, Z. *Science* **2010**, *329*, 61–64.
- (8) Fu, L.; Kane, C. L. *Phys. Rev. Lett.* **2008**, *100*, 096407.
- (9) Chen, Y. L.; Chu, J. H.; Analytis, J. G.; Liu, Z. K.; Igarashi, K.; Kuo, H.-H.; Qi, X. L.; Mo, S. K.; Moore, R. G.; Lu, D. H.; Hashimoto, M.; Sasagawa, T.; Zhang, S. C.; Fisher, I. R.; Hussain, Z.; Shen, Z. X. *Science* **2010**, *329*, 659.
- (10) Wray, L. A.; Xu, S.-Y.; Xia, Y.; Hsieh, D.; Fedorov, A. V.; Hor, Y. S.; Cava, R. J.; Bansil, A.; Lin, H.; Hasan, M. Z. *Nat. Phys.* **2011**, *7*, 32–37.
- (11) Liu, M.; Zhang, J.; Chang, C.-Z.; Zhang, Z.; Feng, X.; Li, K.; He, K.; Wang, L.-L.; Chen, X.; Dai, X.; Fang, Z.; Xue, Q.-K.; Ma, X.; Wang, Y. *Phys. Rev. Lett.* **2012**, *108*, 036805.
- (12) Peng, H.; Lai, K.; Kong, D.; Meister, S.; Chen, Y.; Qi, X.-L.; Zhang, S.-C.; Shen, Z.-X.; Cui, Y. *Nat. Mater.* **2010**, *9*, 225–229.
- (13) Xiu, F.; He, L.; Wang, Y.; Cheng, L.; Chang, L.-T.; Lang, M.; Huang, G.; Kou, X.; Zhou, Y.; Jiang, X.; Chen, Z.; Zou, J.; Shailos, A.; Wang, K. L. *Nat. Nanotechnol.* **2011**, *6*, 216–221.
- (14) Kong, D.; Cha, J. J.; Lai, K.; Peng, H.; Analytis, J. G.; Meister, S.; Chen, Y.; Zhang, H.-J.; Fisher, I. R.; Shen, Z.-X.; Cui, Y. *ACS Nano* **2011**, *5*, 4698–4703.
- (15) Kong, D.; Chen, Y.; Cha, J. J.; Zhang, Q.; Analytis, J. G.; Lai, K.; Liu, Z.; Hong, S. S.; Koski, K. J.; Mo, S.-K.; Hussain, Z.; Fisher, I. R.; Shen, Z.-X.; Cui, Y. *Nat. Nanotechnol.* **2011**, *6*, 705–709.
- (16) Steinberg, H.; Gardner, D. R.; Lee, Y. S.; Jarillo-Herrero, P. *Nano Lett.* **2010**, *10*, 5032–5036.
- (17) Yuan, H.; Liu, H.; Shimotani, H.; Guo, H.; Chen, M.; Xue, Q.; Iwasa, Y. *Nano Lett.* **2011**, *11*, 2601–2605.
- (18) Cha, J. J.; Williams, J. R.; Kong, D.; Meister, S.; Peng, H.; Bestwick, A. J.; Gallagher, P.; Goldhaber-Gordon, D.; Cui, Y. *Nano Lett.* **2010**, *10*, 1076–1081.
- (19) Kong, D.; Randel, J. C.; Peng, H.; Cha, J. J.; Meister, S.; Lai, K.; Chen, Y. L.; Shen, Z. X.; Manoharan, H. C.; Cui, Y. *Nano Lett.* **2010**, *10*, 329–333.
- (20) Kondo, J. *Prog. Theor. Phys.* **1964**, *32*, 37.
- (21) Analytis, J. G.; McDonald, R. D.; Riggs, S. C.; Chu, J.-H.; Boebinger, G. S.; Fisher, I. R. *Nat. Phys.* **2010**, *6*, 960–964.
- (22) Goldhaber-Gordon, D.; Göres, J.; Kastner, M. A.; Shtrikman, H.; Mahalu, D.; Meirav, U. *Phys. Rev. Lett.* **1998**, *81*, 5225–5228.
- (23) Lee, M.; Williams, J. R.; Zhang, S.; Frisbie, C. D.; Goldhaber-Gordon, D. *Phys. Rev. Lett.* **2011**, *107*, 256601.
- (24) Hikami, S.; Larkin, A. I.; Nagaoka, Y. *Prog. Theor. Phys.* **1980**, *63*, 707–710.
- (25) Nomura, K.; Koshino, M.; Ryu, S. *Phys. Rev. Lett.* **2007**, *99*, 146806.
- (26) He, H.-T.; Wang, G.; Zhang, T.; Sou, I.-K.; Wong, G. K. L.; Wang, J.-N.; Lu, H.-Z.; Shen, S.-Q.; Zhang, F.-C. *Phys. Rev. Lett.* **2011**, *106*, 166805.
- (27) Cha, J. J.; Kong, D.; Hong, S.-S.; Analytis, J. G.; Lai, K.; Cui, Y. *Nano Lett.* **2012**, *12*, 1107–1111.
- (28) Chen, J.; He, X. Y.; Wu, K. H.; Ji, Z. Q.; Lu, L.; Shi, J. R.; Smet, J. H.; Li, Y. Q. *Phys. Rev. B* **2011**, *83*, 241304.
- (29) Steinberg, H.; Laloe, J. B.; Fatemi, V.; Moodera, J. S.; Jarillo-Herrero, P. *Phys. Rev. B* **2011**, *84*, 233101.
- (30) Checkelsky, J. G.; Hor, Y. S.; Cava, R. J.; Ong, N. P. *Phys. Rev. Lett.* **2011**, *106*, 196801.
- (31) Altshuler, B. L.; Aronov, A. G.; Khmel'nitsky, D. E. *J. Phys. C* **1982**, *15*, 7367–7386.
- (32) Echternach, P. M.; Gershenson, M. E.; Bozler, H. M. *Phys. Rev. B* **1993**, *48*, 11516–11519.
- (33) Rudolph, M.; Heremans, J. J. *Phys. Rev. B* **2011**, *83*, 205410.
- (34) Beenakker, C. W. J.; van Houten, H. *Phys. Rev. B* **1988**, *37*, 6544–6546.
- (35) Altshuler, B. L.; Aronov, A. G. *Electron-electron interaction in disordered systems*; Elsevier Science Publishing Company: New York, 1985; Vol. 10.
- (36) Lu, H.-Z.; Shi, J.; Shen, S.-Q. *Phys. Rev. Lett.* **2011**, *107*, 076801.
- (37) Hong, S. S.; Cha, J. J.; Kong, D.; Cui, Y. *Nat. Commun.* **2012**, *3*, 757.
- (38) Chang, C.-Z.; Zhang, J.; Liu, M.; Zhang, Z.; Feng, X.; Li, K.; Wang, L.; Chen, X.; Dai, X.; Fang, Z.; Qi, X. L.; Zhang, S. C.; Wang, Y.; He, K.; Ma, X.; Xue, Q. 2011, <http://arxiv.org/abs/1108.4754>.